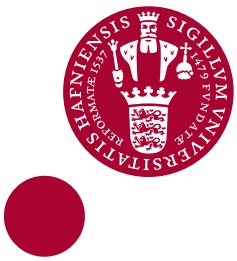

# Gate-dependent orbital magnetic moments in carbon nanotubes

Jespersen, Thomas Sand; Grove-Rasmussen, Kasper; Flensberg, Karsten; Paaske, Jens; Muraki, K.; Fujisawa, T.; Nygård, Jesper

*Published in:*
Physical Review Letters

*DOI:*
10.1103/PhysRevLett.107.186802

*Publication date:*
2011

*Document version*
Early version, also known as pre-print

nature physics

SUPPLEMENTARY INFORMATION

DOI: 10.1038/NPHYS1880

# Supplementary Information
# Gate-dependent spin-orbit coupling in multi-electron carbon nanotubes

T. S. Jespersen, K. Grove-Rasmussen, J. Paaske,
K. Muraki, T. Fujisawa, J. Nygård, and K. Flensberg

**Abstract**

We here present additional theoretical analysis and experimental data supporting the conclusions in the article. First, the carbon nanotube dispersion relation including spin-orbit interaction is reviewed starting from a modified Dirac Hamiltonian, and the single-particle model used in the fitting procedure is explained. Second, tunneling spectroscopy data and the corresponding analysis used to extract the gate-dependent spin-orbit coupling strength are presented.

## Contents

DOI: 10.1038/NPHYS1880

# 1 Carbon nanotube quantum dot with spin-orbit interaction and iso-spin mixing

In this section, we discuss the theory for the spectrum of a carbon nanotube quantum dot and how it is modified by spin-orbit coupling and iso-spin (valley) mixing. The theory is used to fit the spectroscopic data and to extract the values of the spin-orbit coupling and $KK'$ iso-spin mixing terms. Starting from a clean, disorder-free nanotube (*i.e.* no valley mixing), the Hamiltonian near the $K$ and $K'$ points is [1, 2]

$$H_0 = v\left(\tau p_x \sigma_1 + p_y \sigma_2\right) - \Delta_g \sigma_1 + \tau s_y \sigma_1 \Delta^1_{SO} + \tau s_y \Delta^0_{SO} + V(y), \qquad (1)$$

where $\sigma_i,\ i = 1,2,3$ are the Pauli matrices in the $A$-$B$ graphene sub-lattice space, $v$ is the Fermi velocity, and $\tau = \pm 1$ the iso-spin index. Here $p_y$ is the momentum along the tube (coordinate $y$), while $p_x$ is in the circumferential direction (coordinate $x$). The spin is described by the Pauli matrix $s_y$ with eigenvalues $s = \pm 1$ for eigenstates with spins aligned along the nanotube axis, and $V(y)$ is the confining potential along the tube. The curvature induced mass term $\Delta_g$ depends on the diameter $D$ and the chiral angle $\eta$ (defined in the range 0 to 30 degrees with $\eta = 0$ for zigzag tubes), see below. The spin-orbit interaction part of the Hamiltonian has two types of curvature spin-orbit terms: one diagonal and one non-diagonal in $A$-$B$ space. The strength of these are $\Delta^0_{SO}$ and $\Delta^1_{SO}$, respectively. The curvature induced spin-orbit interaction is proportional to $1/D$ and the intra-atomic spin-orbit interaction $\Delta^C_{SO} \simeq 6$-$8\,\mathrm{meV}$ [2, 3], and the diagonal part also depends on the chirality of the tube. Bandstructure calculations [2] give that

$$\Delta^1_{SO} = -\alpha_1 \frac{\Delta^C_{SO}}{D}, \quad \alpha_1 \approx 0.048 \text{ nm} \qquad (2)$$

$$\Delta^0_{SO} = \alpha_2 \frac{\Delta^C_{SO}}{D} \cos(3\eta), \quad \alpha_2 \approx -0.045 \text{ nm} \qquad (3)$$

$$\Delta_g = \frac{\beta}{D^2} \cos(3\eta), \quad \beta \approx 24 \text{ meV}\cdot \text{nm}^2 \qquad (4)$$

These values are results of a tight-binding calculation, with intra atomic spin-orbit interactions only, and should therefore be taken with some caution. In our experiment, we cannot determine $D$ and $\eta$ independently, however, using an estimate for the diameter, we can compare the theoretical band structure parameters $\alpha_1$ and $(\alpha_2/\beta)$ to experimentally estimated values

$$\alpha_1^{exp} = -\frac{\Delta^1_{SO} D}{\Delta^C_{SO}} \qquad (5)$$

$$(\alpha_2/\beta)^{exp} = \frac{\Delta^0_{SO}}{\Delta_g \Delta^C_{SO} D} \qquad (6)$$

using the measured $\Delta^1_{SO}$, $\Delta^0_{SO}$ and $\Delta_g$ as is done in the article.

The eigenstates of $H_0$ are of the form

$$\psi^{\tau} = e^{i\mathbf{K}^{\tau}\cdot\mathbf{r}} e^{ik_x x}\phi^{\tau s}(y). \tag{7}$$

An external magnetic field $B_{||}$ causing an Aharonov-Bohm flux $\Phi$ through a cross-section of the nanotube shifts the wave number by $k_\Phi = 2\Phi/D\Phi_0 = eB_{\|}D/4\hbar$, with $\Phi_0 = h/e$. By imposing periodic boundary conditions along the circumferential direction the wave vector in the $x$-direction becomes $k_x = k_\Phi + 2\tau\nu/3D$, where $\nu$ is 0 or $\pm 1$ depending on the type of tube. For small bandgap tubes, as the situation in the experiment, one has $\nu = 0$.

The longitudinal part of the envelope wave function $\phi^{\tau s}(y)$ depends on the confining potential. Let us assume that there is a large region in the middle of the dot with a constant potential. In this region the wavefunction is a superposition of the two states $\phi^{\tau s}_{\pm} = A_{\pm}\exp(\pm ik_y^{\tau s}y)$, $k_y^{\tau s} > 0$ [4]. The constants $A_\pm$ are determined by the boundary conditions at the ends of dot $y = 0$ and $L$. For a sharp termination of the potential, we have $A_+ \approx -A_-$ and hence $k_y^{\tau s} \approx N\pi/L,\ N = 1, 2, 3, ...$

Choosing the spin quantization axis to be along the tube axis the Hamiltonian $H_0$ is then written as

$$H_0 = \begin{pmatrix} 0 & \hbar v(\tau k_x - ik_y^{\tau s}) \\ \hbar v(\tau k_x + ik_y^{\tau s}) & 0 \end{pmatrix} + \begin{pmatrix} s\tau\Delta^0_{SO} & s\tau\Delta^1_{SO} - \Delta_g \\ s\tau\Delta^1_{SO} - \Delta_g & s\tau\Delta^0_{SO} \end{pmatrix}, \tag{8}$$

and the eigenenergies are

$$E^{\pm}_{\tau,s} = s\tau\Delta^0_{SO} \pm \sqrt{\left(-\Delta_g + \tau\Delta_\Phi + \tau s\Delta^1_{SO}\right)^2 + {\varepsilon_N}^2}, \tag{9}$$

with $\varepsilon_N = \hbar v N\pi/L$, the upper/lower sign referring to conduction or valence band states, and the Aharonov-Bohm energy given as

$$\Delta_\Phi = \hbar v k_\Phi = \frac{evDB_{\|}}{4} = \frac{m\omega_c vD}{4}. \tag{10}$$

In Eq. 9 we have written the eigenenergies in a different (K,K') gauge than that of Ref. [2], which has

$$E^{\pm}_{\tau,s} = s\tau\Delta^0_{SO} \pm \sqrt{\left(-\tau\Delta_g + \Delta_\Phi + s\Delta^1_{SO}\right)^2 + {\varepsilon_N}^2},$$

Finally, in addition to the orbital coupling, the magnetic field also couples to the spin degree of freedom by the Zeeman term

$$H_Z = -\frac{1}{2}\mu_s \mathbf{B}\cdot\mathbf{s}, \tag{11}$$

where $\mu_s = -g_s\mu_B$ and $\mathbf{s}_i$ are the Pauli matrices in spin space. Using the above solutions in absence of $H_Z$ as basis states, the Hamiltonian (for each isospin) is

$$H_0 + H_Z = \begin{pmatrix} E^{\pm}_{\tau,1} - \frac{1}{2}\mu_s B_{\|} & \frac{1}{2}\mu_s B_{\perp} \\ \frac{1}{2}\mu_s B_{\perp} & E^{\pm}_{\tau,-1} + \frac{1}{2}\mu_s B_{\|} \end{pmatrix}, \tag{12}$$

which is readily diagonalized.

DOI: 10.1038/NPHYS1880

## 1.1 The spectrum for parallel magnetic field

For the magnetic field parallel to the tube axis and $\Delta_g \gg |\Delta_{SO}^0|, |\Delta_{SO}^1|, |\Delta_\Phi|$ the energy of the four states in the quantum dot is to linear order in $B_\parallel$ given by

$$E_{\tau,s}^{\parallel,\pm} \approx E_0^\pm + s\tau\frac{\Delta_{SO}}{2} + \Big(\frac{1}{2}g_s s \mp \tau g_{\rm orb}\Big)\mu_B B_\parallel \tag{13}$$

with $g_s = 2$, $E_0^\pm = \pm\sqrt{\Delta_g^2 + \varepsilon_N^2}$ and

$$g_{\rm orb} = \frac{evD}{4\mu_B\sqrt{1+(\frac{\varepsilon_N}{\Delta_g})^2}} \tag{14}$$

$$\Delta_{SO} = 2\Big(\Delta_{SO}^0 \mp \frac{\Delta_{SO}^1}{\sqrt{1+(\frac{\varepsilon_N}{\Delta_g})^2}}\Big) \tag{15}$$

What is measured is $|\Delta_{SO}|$, and the sign of $\Delta_{SO}$ can be inferred from the magnetic field dependence as follows. The doublet with parallel spin and orbital magnetic moments consists of the states with the largest slope in $B_\parallel$ and thus requires that the sign of the $g_{\rm orb}$ and $g_s$-terms are the same in Eq. 13, *i.e.* $\mp\tau = s$ or equivalently $s\tau = \mp 1$. Whether these states constitute the lower or the excited doublet (for $B_\parallel = 0$) is determined by the sign of the energy shift due to the second term of Eq. 13: $\mathrm{sign}(s\tau\Delta_{SO}) = s\tau\mathrm{sign}(\Delta_{SO}) = \mp\mathrm{sign}(\Delta_{SO})$. Thus a negative/positive sign of $\Delta_{SO}$ will make this doublet the ground state in the valence/conduction band - the resulting level structure in the two cases is illustrated in Fig. S1 with the red lines showing the above discussed doublet. Our measurement corresponds to the rightmost panel for both conduction and valence band states, that is

$$\Delta_{SO} > 0 \tag{16}$$

For the measurements in Ref. [3], $\Delta_{SO}$ is positive for the conduction band and negative for the valence band. The separate contributions of $\Delta_{SO}^0$ and $\Delta_{SO}^1$ is determined by fitting the $\Delta_{SO}$ values (with sign inferred as above) to Eq. 15 as discussed in the main article.

## 1.2 Including disorder

Since isospin mixing is an experimentally very important effect, this must be included in the modelling of the quantum dot spectrum to correctly describe the data. The microscopic nature of the sources to $KK'$ mixing is in general unknown, but several factors can contribute to the mixing, *e.g.,* couplings to the substrate which breaks rotational invariance, a random distribution of defects in the tube, or end effects for non-adiabatic confining potentials. In our basis for the clean wire, these effects result in matrix elements $\Delta_{KK'} = \langle s\tau|H_{KK'}|s\bar{\tau}\rangle$ (notice that spin is conserved, assuming non-magnetic symmetry breaking only). Therefore, with $KK'$ mixing included, the Hamiltonian within a single nanotube

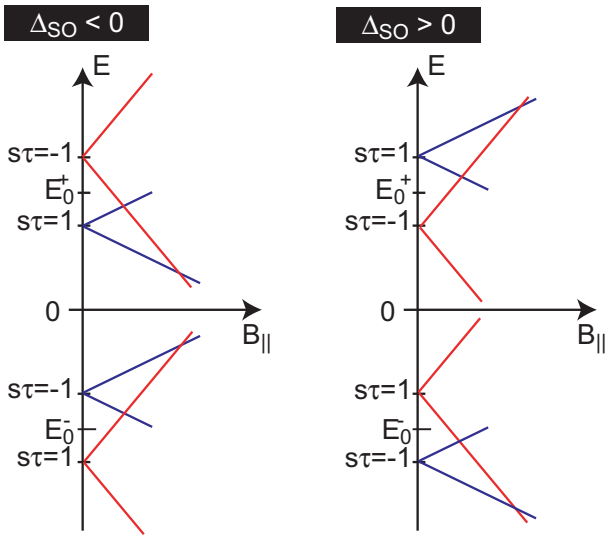


Figure S1: Energy diagrams of conduction and valence band quartets used for identifying the sign of the measured $\Delta_{SO}$. For negative $\Delta_{SO}$, Eq. 13 dictates that the ground state doublet in the conduction band has $s\tau = 1$. This requirement on the quantum numbers results in different sign on the $g_{orb}$ and $g_s$-terms yielding the weaker slope in $B_{\|}$. Similarly, for the valence band the doublet ground state has $s\tau = 1$, but now the $g_{orb}$ and $g_s$-terms have the same sign giving the larger slope in $B_{\|}$. In case of positive spin-orbit coupling, the doublets in each Kramers doublet is interchanged as seen from Eq. 13.

DOI: 10.1038/NPHYS1880

shell in a magnetic field having an angle $\theta$ relative to the tube axis is (using the basis $(K\uparrow_y, K'\downarrow_y, K\downarrow_y, K'\uparrow_y)$)

$$H = \begin{pmatrix} E^{\pm}_{1,1} & 0 & 0 & \Delta_{KK'} \\ 0 & E^{\pm}_{-1,-1} & \Delta_{KK'} & 0 \\ 0 & \Delta_{KK'} & E^{\pm}_{1,-1} & 0 \\ \Delta_{KK'} & 0 & 0 & E^{\pm}_{-1,1} \end{pmatrix} + \frac{1}{2} g\mu_B B \begin{pmatrix} \cos\theta & 0 & \sin\theta & 0 \\ 0 & -\cos\theta & 0 & \sin\theta \\ \sin\theta & & -\cos\theta & 0 \\ 0 & \sin\theta & 0 & \cos\theta \end{pmatrix}. \quad (17)$$

The energies in the diagonal $E^{\pm}_{\tau,s}$ are generally given by Eq. 9, but fullfilling the requirement of the expansion in Eq. 13, we use this simpler form $E^{\parallel,\pm}_{\tau,s}$ omitting the Zeeman term $\frac{1}{2}gs$ and substituting the parallel field by $B_{\parallel} = B\cos\theta$. After diagonalizing H we can thus fit the experimentally observed spectrum, using $\Delta_{SO}$, $\Delta_{KK'}$ and $g_{orb}$ as fitting parameters.

### 1.3 Two-electron spectrum

In absence of exchange coupling the two-electron spectrum is simply given by filling up the one-electron states found above. We classify these according to their spectroscopic nature, i.e., how they split in a magnetic field and denote them therefore as singlet- and triplet-like states. They are not singlets and triplets in the usual sense of spin singlets and triplets.

## 2 Supplementary data

A central point of our work is that of Fig. 4a in the article, which shows the gate voltage-dependence of the effective spin-orbit coupling strength $\Delta_{SO}$. Each data point in the figure is obtained by fitting the single-particle energy spectrum to magnetic field dependent tunneling spectroscopy measurements. This section presents the analysis of the underlying data. We start by discussing results from the conduction band where both sequential- and cotunneling spectroscopy have been performed (Sec. 2.1). Subsequently, we present data from the valence band where a positive value of $\Delta_{SO}$ is found by cotunneling spectroscopy (Sec. 2.2).

### 2.1 Conduction band

The spin-orbit parameter $\Delta_{SO}$ has been extracted from 14 shells in the conduction band labeled A-N with shell A(N) corresponding to the lowest(highest) positive gate voltage. Shell E at $V_g \approx 5.6 - 5.7\,\mathrm{V}$ corresponds to the quartet for which the cotunneling spectroscopy was analyzed in Fig. 3 of the article. For lower gate voltages, the lead-nanotube Schottky barrier is larger, significantly

decreasing the cotunneling current and for shells A and B cotunneling spectroscopy is no-longer feasible. Instead we show in section 2.1.1 how sequential tunneling spectroscopy also yields the effective spin-orbit coupling strength in complete accordance with the single-particle model. The additional 12 shells (C-N) in the conduction band allow cotunnelling spectroscopy as presented in section 2.1.2.

### 2.1.1 Sequential tunneling spectroscopy

The electron filling of quantum states for smaller gate voltages than shown in Fig. 1b in the article is analyzed in Fig. S2a-b. They show the stability diagram (S2b) with relatively weak lead-dot tunnel-coupling and the corresponding addition energies (S2a) extracted from the widths of the diamonds (and scaled by the gate coupling factor). The large addition energy for every fourth electron (red data points in Fig. S2a) clearly shows the regular four-electron shell filling, which persists over many electronic shells. A zoom of the two shells labeled A and B is shown in Fig. S2c. Due to the weak coupling, gate-independent cotunneling steps are not observed. Instead, lines parallel to the diamond edges representing sequential transport through excited states of the charge-state at which they terminate are well resolved and can thus be used for spectroscopy. The linewidth $\approx$ 200-300 $\mu$eV is determined by the tunnel coupling of the quantum dot to the leads and sets the energy resolution of the measurement. Figure S2d shows the transconductance $dI/dV_g$ vs. $V_{sd}$ and energy ($V_g$) around the $4N_1 \sim 120$ electron charge state with $N_1$ completely filled four-electron shells as marked in Fig. S2c. The Coulomb diamonds are clearly observed and at the upper (lower) crossing point one electron is added (removed) to the next empty (last filled) quartet. Note, that by measuring transconductance (rather than $dI/dV_{sd}$), the lines acquire an additional sign reflecting levels entering(positive $dI/dV_g$) or leaving(negative) the available bias window [5]. This feature eases the identification of the relevant levels in Fig. S2e, where traces along the black line at fixed bias $V_{sd} = 4\,\mathrm{mV}$ are measured while varying $B_\parallel$. Consider first the spectrum of the $4N_1 + 1$ charge state (shell B). Increasing $B_\parallel$ the doubly degenerate ground-state splits into two states ($\alpha$,$\beta$) while the excited states ($\gamma, \delta$) steeply separates from the ground-state but are only discernably split at $B_\parallel \approx 3\,\mathrm{T}$ as emphasized in the inset. As discussed in the article, this asymmetry is a direct consequence of SOI (see Fig. 2d in the article) and the measurements are accurately reproduced by the calculation overlaid on the $B_\parallel > 0$ part of Fig. S2e with $\Delta_{SO} = 0.2\,\mathrm{meV}$, $\Delta_{KK'} = 0.58\,\mathrm{meV}$, and $g_{\mathrm{orb}} = 7.8$. Importantly, even though the SOI is masked in the low field regime by the dominating disorder and the limited spectroscopic resolution, it clearly stands out in the high field regime as the asymmetry of the splitting of the two doublets ($\alpha, \beta$) vs. ($\gamma, \delta$). The corresponding evolution for the $4N_1 - 1$ charge state is similar (shell A), and is fitted with the same values for $\Delta_{SO}$ and $g_{\mathrm{orb}}$ and taking $\Delta_{KK'} = 0.75\,\mathrm{meV}$.

Figure S2f shows the corresponding measurement in a perpendicular field $B_\perp$. The level structure is in complete agreement with the model which does not contain any free parameters. Since $\Delta_{SO}$ is below the spectroscopic res-

DOI: 10.1038/NPHYS1880

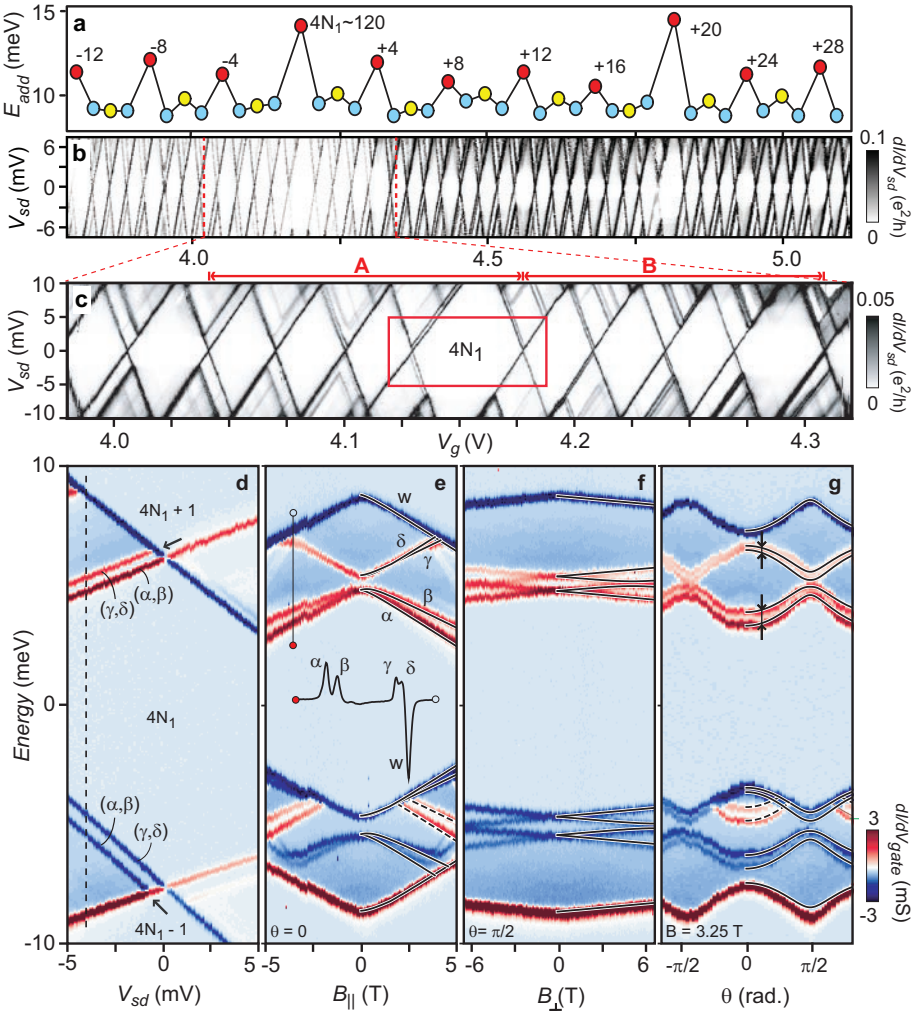


Figure S2: **a**, Addition energy as a function of $V_g$ extracted from the stability diagram in **b** revealing consecutive four-electron shell filling for a large number of shells. **c**, Charge stability diagram of the two shells (A & B) in which the sequential tunneling analysis is made for 3 and 1 electrons in the two shells, respectively. **d**, Transconductance $dI/dV_g$ vs. $V_g$ and $V_{sd}$ around a full electron shell $4N_1 \approx 120$. Upper(lower) arrow indicates the first excited state of the first(last) electron in an otherwise empty(filled) shell. **e**, Transconductance along the dashed line in **d** at $V_{sd} = 4\,\mathrm{mV}$ measured as a function of parallel magnetic field. Inset shows a cut along the vertical line emphasizing the asymmetric splitting of the two doublets; $(\alpha, \beta)$ vs. $(\gamma, \delta)$ which is the consequence of SOI. Labels $\alpha$, $\beta$, $\gamma$, $\delta$ refer to Fig. 2d in the article. **f**, As **d** but applying the magnetic field perpendicular to the axis; the doublets split equally. **g**, Measurements in a constant magnetic field $B = 3.25\,\mathrm{T}$ while varying the angle $\theta$ between $B$ and the CNT axis. In **e-g** the solid lines are a single fit to the theory with a total of only four parameters $\Delta_{SO} = 0.2\,\mathrm{meV}, g_{\mathrm{orb}} = 7.8$ and $\Delta_{KK'} = 0.58(0.75)\,\mathrm{meV}$ for the $4N_1 + 1(4N_1 - 1)$ charge state. The theory has been overlaid only for $B > 0$ not to mask the data. Dashed lines in **e** and **g** are excitations belonging to the $4N_1 + 1$ charge state also anticipated by the model with a level-spacing of 6 meV.

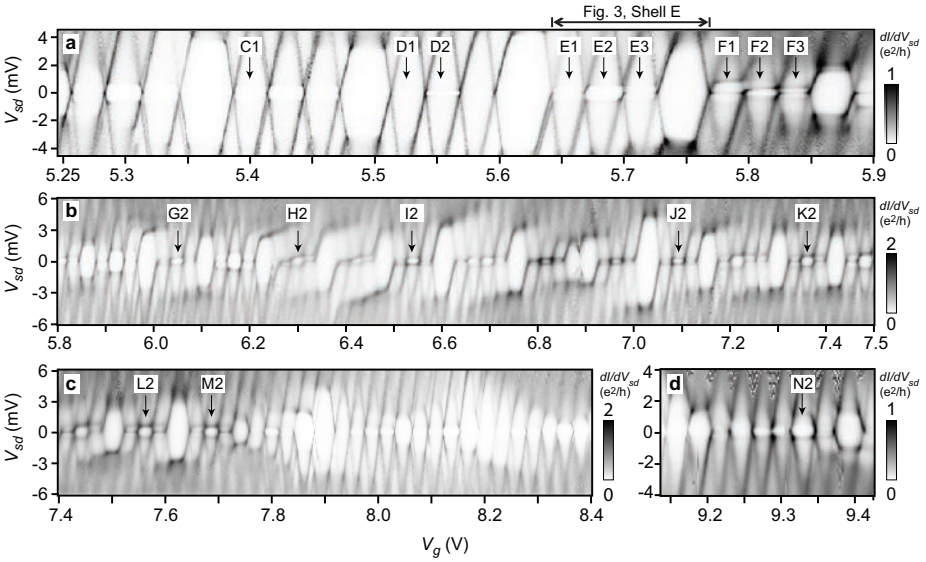


Figure S3: **a-d**, Charge stability diagrams at higher gate voltages with the CNT quantum dot being in the cotunneling regime. Arrows point to charge states where cotunneling spectroscopy have been measured (see Figs. S4 and S5). The shell labeled E is analyzed in details in Fig. 3 of the article.

olution the avoided crossing cannot be clearly discerned in the measurement (unlike the case for the cotunneling measurements in Fig. 3 in the article). For completeness we show in Fig. S2g the spectrum for fixed $B = 3.25\,\mathrm{T}$ while continuously varying the angle $\theta$ between the nanotube and the field. Here the presence of SOI is responsible for the angle dependence of the internal doublet splittings (arrows), and again the model is in near-perfect agreement with the data without any free parameters.

### 2.1.2 Cotunneling spectroscopy

For higher gate voltages, as already mentioned, the tunnel coupling to the electrodes increases, and allows for inelastic cotunneling spectroscopy. As shown in Fig. 3 in the article, the spin-orbit coupling can in this case be directly read-off by avoided level crossings in perpendicular magnetic field for 1, 2, and 3 electrons. Moreover, the spin-orbit coupling breaks the intra-shell electron-hole symmetry, which can be probed by comparing the 1 and 3 electron cases in parallel field. Figures S3a-d show charge stability diagrams in the cotunneling regime, where arrows point to charge states for which field-dependent cotunneling spectroscopy has been performed. In Fig. S3b-d, the level broadening due to electrode-dot coupling is even stronger and the spin-orbit coupling is extracted from the avoided crossing (of magnitude $2\Delta_{SO}$) between the two-

DOI: 10.1038/NPHYS1880

electron singlet-like $\tilde{S}_0$ and triplet-like $\tilde{T}_-$ states in perpendicular field.

Figure S4 shows cotunneling spectroscopy plots ($d^2I/dV_{sd}^2$ versus gate and magnetic field) of shells C, D and F in the cotunneling regime marked in Fig. S3a. The overall features reproduce Fig. 3 in the article and show excellent agreement with the model (black lines). Parameters used in the fits are all summarized in Table S1. We now comment on the details observed in each shell, and on how the spin-orbit strength and other parameters are found.

Shell C is analyzed in Figs. S4a-b, which show cotunneling spectroscopy for 1 electron in perpendicular and parallel magnetic fields. The spin-orbit coupling is directly estimated in Fig. S4a from the avoided crossing at $B = \pm 4.5\,\mathrm{T}$ yielding $\Delta_{SO} \simeq 140\,\mu\mathrm{eV}$. Furthermore, the orbital coupling $\Delta_{KK'} \simeq 495\,\mu\mathrm{eV}$ and $g_{orb} \simeq 5.7$ are chosen to produce the theoretical predicted excitations, which perfectly match the observed threshold of inelastic cotunneling (peaks and dips).

Measurements of shell D is displayed in Figs. S4c-g which show a different behavior than shell C, because the orbital coupling is smaller than the spin-orbit coupling. The spin-orbit coupling for this shell is extracted in Fig. S4d from the avoided crossing between $\tilde{S}_0$ and $\tilde{T}_-$ states in case of the two-electron cotunneling spectroscopy in perpendicular magnetic field. The theory matches the experimental data except in Fig. S4d, where some small deviations are observed at high fields. All other figures show good agreement between theory and experiment, most remarkably in Fig. S4g, where the sample is rotated to an angle of 22.5 degrees between the nanotube axis and the magnetic field. Note, that the theory lines in Fig. S4e-g at negative biases are only plotted for low fields to clearly reveal the underlying data.

Shell F is presented in Figs. S4h-m, which show the magnetic field dependence in parallel and perpendicular magnetic fields for fillings 1-3 (as in Fig. 3 in the article). The overall conductance in this shell is higher than for the shells analyzed above. Moreover, the zero-field threshold of inelastic cotunneling is seen to vary with filling, which is not fully accounted for in our model. The clear avoided crossing for 2 electrons in perpendicular magnetic field (Fig. S4i), and the breaking of electron-hole symmetry in parallel magnetic field for electron fillings 1 and 3 (Figs. S4k,m) unambiguously reveal the spin-orbit interaction. Interestingly, for 2 electrons, four (not three as in Fig. 3 in the article) excitation lines are seen to emerge from the zero field peak at $V_{sd} = 0.25\,\mathrm{meV}$ in Fig. S4i. Such behavior is indeed expected in the presence of finite exchange interaction ($J > 0$), which splits the $\tilde{S}_1$ and $\tilde{T}$ states. The deviation between experiment and theory at large $B_\parallel$ in Fig. S4l may be attributed to avoided crossings with states from the next shell. The fitting parameters are chosen to mainly match the inelastic cotunneling thresholds of Figs. S4h (not S4j) and S4i. A more detailed analysis of CNT two-electron physics including exchange, disorder and spin-orbit interaction will be presented elsewhere.

For shells G-N (Fig. S3) the lead-dot coupling is even stronger, leading to pronounced Kondo physics for 1 and 3 electron fillings and Kondo enhanced inelastic cotunneling at half filling [6]. Figure S5 shows two-electron cotunneling spectroscopy for perpendicular magnetic field. The orbital coupling $\Delta_{KK'}$ is found from the zero-field splitting $\Lambda$ between the two Kramers doublets (green

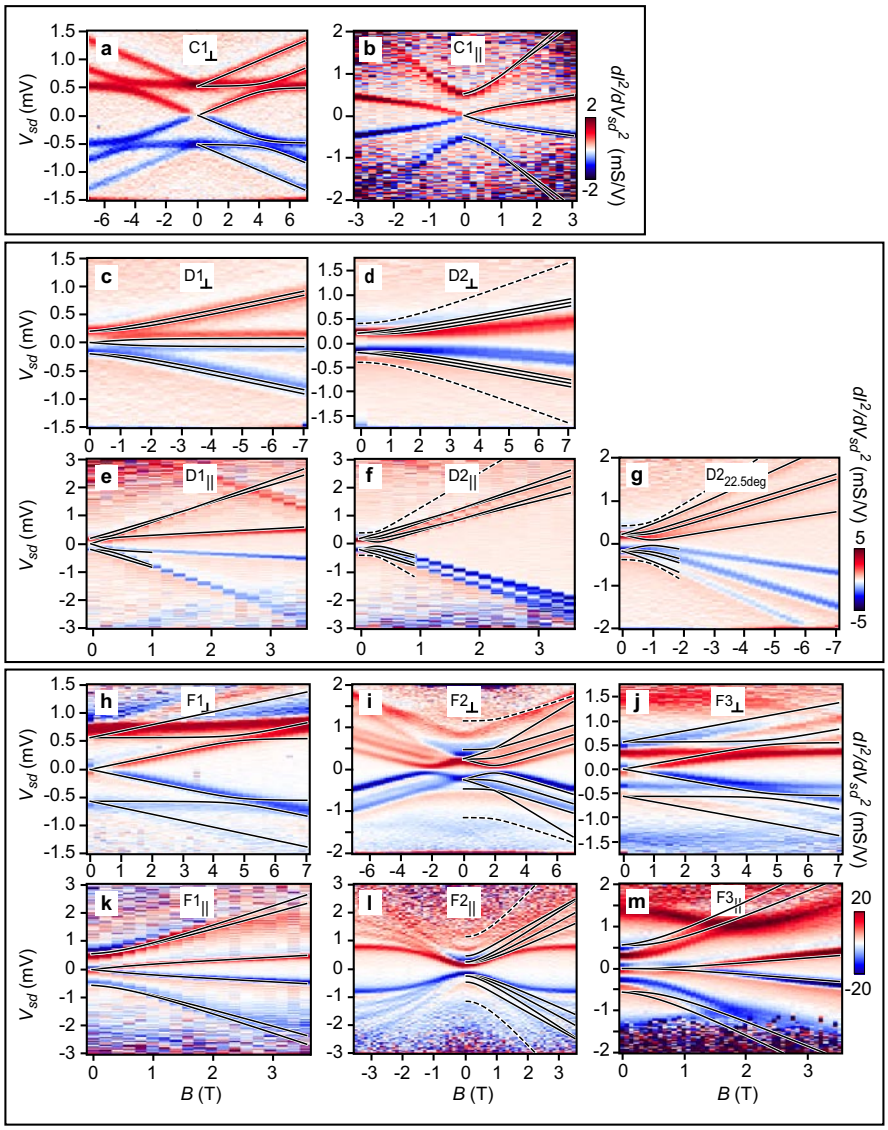


Figure S4: Cotunneling spectroscopy $d^2I/dV_{sd}^2$ versus bias and magnetic field for shell C (**a,b**), D (**c-g**) and F (**h-m**). The labels indicate shell and electron filling in correspondence with Fig. S3a as well as orientation of the field relative to the carbon nanotube axis. Data are acquired at gate voltages corresponding to the center of the respective Coulomb diamond. The lines display the excitation spectrum, (*i.e.,* threshold of inelastic cotunneling) predicted by the single- and two-particle model having four independent parameters, the orbital coupling (disorder) parameter $\Delta_{KK'}$, the spin-orbit coupling $\Delta_{SO}$, the orbital $g$-factor $g_{orb}$ and the exchange interaction $J$. Parameters are summarized in Table S1.

DOI: 10.1038/NPHYS1880

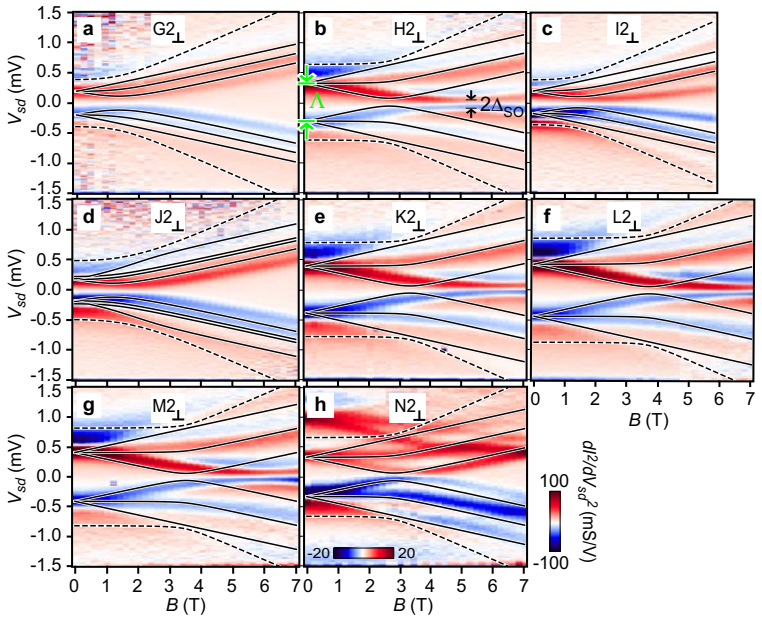


Figure S5: **a-h**, Cotunneling spectroscopy $dI^2/dV_{sd}^2$ versus bias and perpendicular magnetic field at half filling for shells G-N (see stability diagrams in Fig. S3b-d). The spin-orbit coupling $\Delta_{SO}$ is estimated from the avoided crossing between the singlet-like $\tilde{S}_0$ and the triplet-like $\tilde{T}_-$ states as shown in Panel b. The zero field energy difference $\Lambda$ between the ground and excited Kramers doublets allows the calculation of the orbital coupling parameter $\Delta_{KK'}$. The lines represent the calculated spectrum of the two-particle model using the two parameters $\Delta_{SO}$ and $\Delta_{KK'}$ as well as a finite exchange $J$. The deviations from the model is attributed to $g$-factor renormalization caused by Kondo correlation which are important in the strongly coupled regime (see text). Note, that the color-scale bar for shell N is different than for shells G-M.

arrows in Panel b), and the spin-orbit coupling appears as the zero bias avoided crossing between the $\tilde{S}$ and $\tilde{T}$ states (black arrows in Panel b). Given these two parameters for each shell the two-electron excitation spectrum is calculated as shown by the black lines. Interestingly, for shells H-M, the $\tilde{S}$-$\tilde{T}$ avoided crossings occur at somewhat higher magnetic fields than predicted. This is consistent with correlation induced renormalization (lowering) of the $g$-factor [7]. As the coupling is decreased in case of shell N, the correspondence between the model and the experimental threshold of cotunneling is improved confirming that the effect is related to the coupling and not the electron filling. The $g$-factor renormalization is an interesting topic for detailed study and the good understanding of the single-particle spectrum of single wall carbon nanotube electronic shells constitutes an optimal starting point for further explorations.

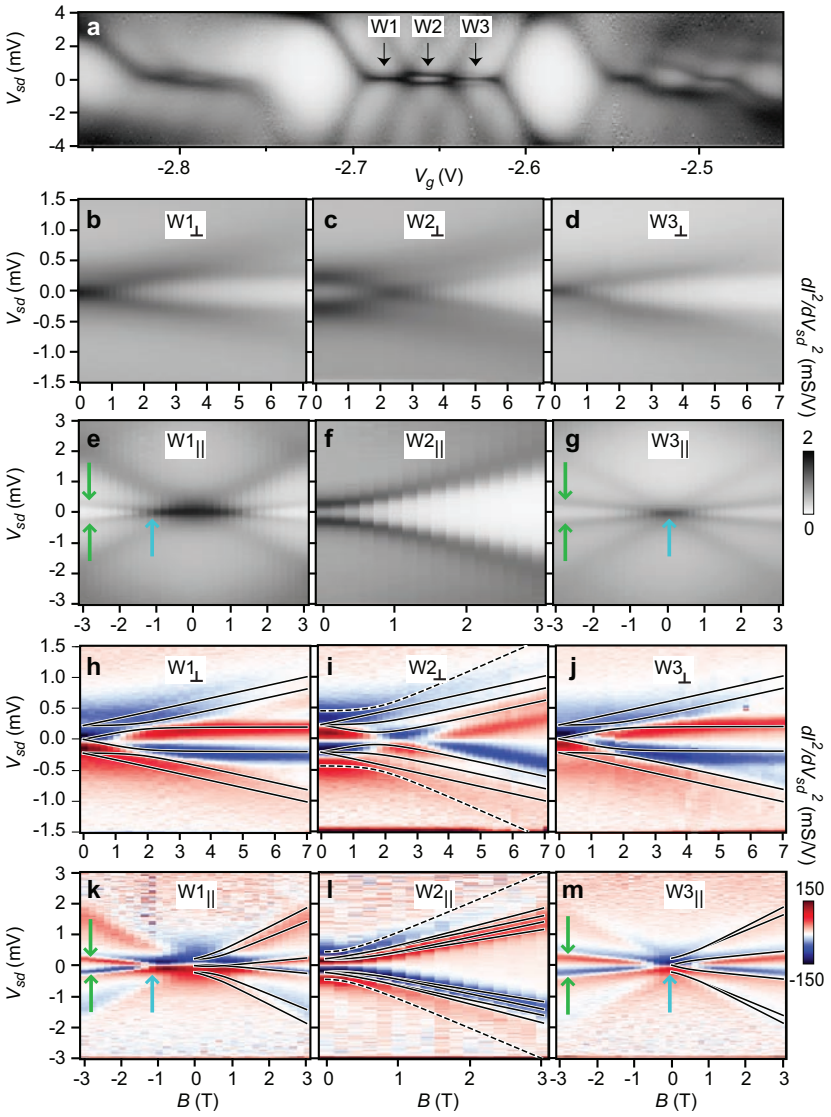


Figure S6: **a**, Stability diagram showing four-electron shell structure in the valence band, where the arrows indicate electron filling 1-3 in shell W. We here consider electron filling in the valence band shell instead of hole filling to make easier comparison to the measurements analyzed in the conduction band. Measured $dI/dV_{sd}$ versus bias and perpendicular/parallel (**b-d**)/(**e-g**) magnetic field for electron filling 1, 2 and 3. Numerically obtained $d^2I/dV_{sd}^2$ versus bias and perpendicular/parallel (**h-j**)/(**k-m**) magnetic field. The green arrows in **e**, **k**, **g**, **m** point to the threshold of inelastic cotunneling involving the ground- and first excited states. The blue arrows indicate the magnetic field for which this threshold is zero. This occurs for $B_{||} \simeq 1\,\mathrm{T}$ and $B_{||} = 0\,\mathrm{T}$ for fillings 1 and 3, respectively, thereby revealing a positive spin-orbit coupling. The parameters used in the calculated spectrum (lines in (**h-m**)) are given in Table S1.

DOI: 10.1038/NPHYS1880

## 2.2 Valence band

For negative gate voltages transport is carried by holes in the valence band of the small-band-gap semiconducting carbon nanotube. The coupling to the electrodes is significantly stronger than for the conduction band and Kondo physics dominates as seen in Fig. S6a. Cotunneling spectroscopy in perpendicular and parallel magnetic field is measured for 1, 2 and 3 electrons in one of the weakest coupled shell W (see arrows). For completeness, both differential conductance $dI/dV_{sd}$ (S6b-g) and its derivative $d^2I/dV_{sd}^2$ (S6h-m) are shown. Due to significant level broadening of the cotunneling features, the (avoided) crossing in perpendicular magnetic field for two electrons results in a singlet-triplet Kondo resonance as seen in Figs. S6c,i [8], and the spin-orbit coupling cannot be directly extracted as the case for weaker coupling (Fig. S5). Instead, we focus on the parallel magnetic field dependence for electron filling 1 and 3. In presence of orbital coupling ($\Delta_{KK'} > 0$) and positive spin-orbit coupling ($\Delta_{SO} > 0$) in the conduction band as discussed in the article, the lines corresponding to the lowest excitation cross zero bias only at $B = 0$ for electron filling 1, while a crossing also occurs at finite parallel magnetic fields for filling 3 (see Fig. 3d,f in the article and Fig. S4k,m). Similar behavior is seen for shell W in Fig. S6k, m where the one and three electron behavior now is interchanged: the cotunneling thresholds corresponding to the lowest excitation (green arrows in Fig. S6e, k) cross at finite fields for filling 1 (blue arrow). Since the quartet is in the valence band, this also corresponds to a positive spin-orbit coupling $\Delta_{SO}$ as seen from Fig. S7 showing the effect negative/positive $\Delta_{SO}$ on the level structure in the valence band (see also Fig. S1). The theoretically expected cotunneling thresholds are indicated by the black lines in Fig. S5 with the values of the orbital coupling and the spin-orbit coupling listed in Table S1. As discussed in the article, a positive spin-orbit coupling is consistent with the expectation from the

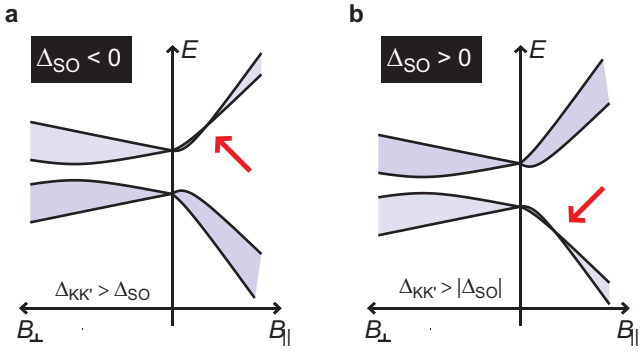


Figure S7: Valence band energy diagrams of quartet with negative (**a**) and positive (**b**) spin-orbit coupling resulting in an interchange of the two Kramers doublets (red arrows). Note, that the sign of $\Delta_{SO}$ would be opposite in case of a quartet in the conduction band as illustrated in Fig. S1.

Dirac band structure, and our measurements at large gate voltages illustrate a different behavior than previously reported, which found a positive/negative spin-orbit coupling for the first quartet in the conduction/valence band [3]. We note, that our device, however, is expected to be similar to that of Ref. [3] for quartets closer to the band gap.

The analysis is repeated for shells Y and Z at larger negative gate voltages presented in Fig. S8a, where the asymmetry between the 1 and 3 electron behavior is observed in Figs. S8b-e. By comparing to theory (black lines) we find a spin-orbit coupling strength $\sim 75\,\mu$V for both shells. Finally, we show that the spin-obit coupling also is observed in stability diagrams as an asymmetric splitting of the 1 and 3 electron Kondo resonances in parallel magnetic fields. This is illustrated in Fig. S8f showing a stability diagram of the three shells X, Y and Z at $B_{\|} = 2\,$T, where an asymmetric splitting of the Kramers doublets for filling 1 and 3 is clearly revealed. The alternating behavior of small and large splitting is highlighted by pairs of yellow and blue arrows. In the case of shell Y the difference in splittings is $\sim 90\,\mu$V, consistent with the spin-orbit coupling strength deduced above. We therefore conclude that also shell X has a positive spin-orbit coupling in the same order as shell Y and Z.

## References

[1] J. Jeong and H. Lee, Phys. Rev. B **80** (2009).

[2] W. Izumida, K. Sato, and R. Saito, J. Phys. Soc. Jpn. **78**, 074707 (2009).

[3] F. Kuemmeth, *et al.*, Nature **452**, 448 (2008).

[4] D. V. Bulaev, B. Trauzettel, and D. Loss, Phys. Rev. B **77**, 235301 (2008).

[5] L. Kouwenhoven, D. Austing, and S. Tarucha, Rep. Prog. Phys. **64**, 701 (2001).

[6] J. Paaske, *et al.*, Nature Physics **2**, 460 (2006).

[7] A. C. Hewson, J. Bauer, and W. Koller, Phys. Rev. B **73**, 045117 (2006).

[8] J. Nygård, D. H. Cobden, and P. E. Lindelof, Nature **408**, 342 (2000).

DOI: 10.1038/NPHYS1880

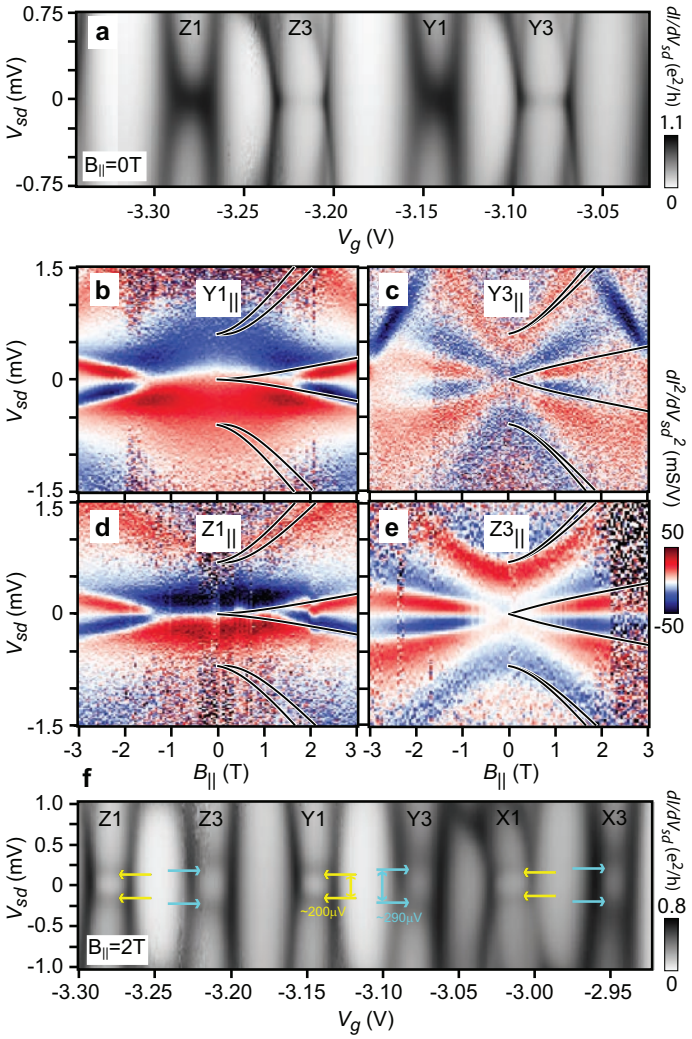


Figure S8: **a**, Stability diagram of shells Y and Z in the valence band from a different cooldown of the same sample. **b-e**, Cotunneling spectroscopy $d^2I/dV_{sd}^2$ versus $V_{sd}$ and parallel magnetic field of shell Y and Z showing the breaking of electron-hole symmetry reflecting a positive spin-orbit coupling strength, *i.e.,* the lowest excitation lines cross at respectively finite and zero field for **b,d** and **c,e**. The black lines are the expected excitations given the parameters in Table S1. (f) Stability diagram at $B_{\parallel} = 2\,\mathrm{T}$ showing shells X, Y, and Z. The spin-orbit interaction is revealed by a difference in splitting of the Kondo resonance for 1 and 3 electrons in a shell (yellow and blue arrows). A spin-orbit interaction of similar strength is therefore inferred also for shell X.

| Shell # | $V_{gate}$(V) | $\Lambda(\mu$eV) | $\Delta_{SO}(\mu$eV) | $\Delta_{KK'}(\mu$eV) | J($\mu$eV) | $g_{orb}$ |
|---|---|---|---|---|---|---|
| A | 4.12 | 775 | 200 | 750 | - | 7.8 |
| B | 4.25 | 615 | 200 | 580 | - | 7.8 |
| C | 5.40 | 515 | 140 | 495 | - | 5.7 |
| D | 5.55 | 200 | 185 | 75 | 0 | 5.5 |
| E (Fig. 3) | 5.68 | 475 | 150 | 450 | 0 | 5.7 |
| F | 5.78 | 560 | 100 | 550 | 450 | 5.4 |
| G | 6.04 | 195 | 115 | 155 | - | - |
| H | 6.30 | 315 | 65 | 310 | - | - |
| I | 6.57 | 190 | 95 | 165 | - | - |
| J | 7.09 | 245 | 125 | 210 | 100 | - |
| K | 7.36 | 390 | 60 | 385 | - | - |
| L | 7.56 | 435 | 60 | 430 | - | - |
| M | 7.69 | 410 | 60 | 405 | - | - |
| N | 9.34 | 330 | 65 | 325 | - | - |
| W | -2.67 | 225 | 100 | 200 | 0 | $\simeq 4.4$ |
| X | -2.98 | - | $\simeq 75$ | - | - | - |
| Y | -3.14 | $\simeq 605$ | $\simeq 75$ | $\simeq 600$ | - | $\simeq 5.8$ |
| Z | -3.25 | $\simeq 705$ | $\simeq 75$ | $\simeq 700$ | - | $\simeq 5.8$ |

Table S1: Parameters extracted for each measured shell in the conduction (A-N) and valence (W-Z) band. Shells A and B are the only shells analyzed in the sequential tunneling regime (Fig. S2), while C-F are in the weak cotunneling regime (Fig. S4 and Fig. 3). As the level-broadening increases even further (G-N), the spin-orbit coupling $\Delta_{SO}$ and the energy splitting between the two Kramers doublets $\Lambda$ is estimated at half filling by the zero-bias avoided crossing at finite magnetic field and the zero-field inelastic cotunneling threshold, respectively (see Fig. S5b). The orbital coupling is related as $\Delta_{KK'} = \sqrt{\Lambda^2 - \Delta_{SO}^2}$, and in some cases a $\tilde{S}_0$-$\tilde{T}$ splitting caused by exchange interaction $J$ can be observed ($J = 0$ means that the exchange interaction is smaller than the spectroscopic line width in the shell). In the valence band, the spin-orbit coupling is observed by the breaking of electron-hole symmetry for 1 and 3 electrons in a parallel magnetic field (S6 and S8). The uncertainty of the spin-orbit coupling strength is shown in Fig. 4 in the article. The dashes indicate that measurement have not been made to extract the corresponding parameter. Note, that the decreasing values of $g_{orb}$ versus gate voltage (filling) in the conduction band is consistent with Eq. 14. As expected the orbital coupling $\Delta_{KK'}$ shows no gate voltage correlation.